International Journal of Greenhouse Gas Control 34 (2015) 39–51

Contents lists available at ScienceDirect

International Journal of Greenhouse Gas Control

journal homepage: www.elsevier.com/locate/ijggc

Parallel simulation of fully-coupled thermal-hydro-mechanical processes in CO_2 leakage through fluid-driven fracture zones

Zhao-Qin Huang[a,b], Philip H. Winterfeld[b], Yi Xiong[b], Yu-Shu Wu[b], Jun Yao[a,*]

[a] School of Petroleum Engineering, China University of Petroleum (East China), Qingdao, China
[b] Department of Petroleum Engineering, Colorado School of Mines, Golden, CO, USA

ARTICLE INFO

Article history:
Received 15 July 2014
Received in revised form 1 November 2014
Accepted 19 December 2014
Available online 19 January 2015

Keywords:
CO_2 leakage
Fluid-driven fracture
Thermal-hydro-mechanical coupling
Fully-coupled simulation
Parallel computing

ABSTRACT

The safety of CO_2 storage in geological formations relies on the integrity of the caprock. However, the elevated fluid pressure during CO_2 injection changes the stress states in the caprock, and may lead to reactivate pre-existing fractures or even fracture the caprock. It is necessary to develop an efficient and practical monitor technology to detect and identify CO_2 leakage pathways. To this end, we should understand the transport behavior of CO_2 coupled with geomechanical effects during injection. In this work, we first developed an efficient parallel fully-coupled thermal-hydro-mechanical simulator to model CO_2 transport in porous media. The numerical model was verified through classical problems with analytical solutions. Then, based on this simulator, we investigated the fluid flow behavior when CO_2 leakage occurs through fluid-driven fracture zones. We proposed an implicit, physics-based model to simulate the fluid-driven fracturing process by using several practical correlations, including fracturing pressure functions, porosity/permeability–stress relationships. A set of numerical simulations have been conducted by considering various scenarios, such as different injection rates, locations and distributions of fracture zones, and initial fracture permeability. The results show that there are several characteristics can be used to detect CO_2 leakage pathways, and it is possible to develop an advanced inverse modeling and monitoring technology to identify leakage locations, times and rates using measured pressure data of permanent downhole gauges and our simulator.

1. Introduction

To address the increasing concerns regarding greenhouse gas emission and its impact on global climate, CO_2 geologic sequestration is considered to be among the most promising, viable approaches for near-term implementation (Bolster, 2014; Huppert and Neufeld, 2014). Carbon dioxide can be sequestered in several types of geological media including deep saline aquifers, depleted oil and gas reservoirs, and coal beds. To achieve significant reduction of atmospheric emissions, large amounts of CO_2 need to be injected into geologic storage reservoirs, leading to pressure buildup and significant changes in formation stress. CO_2 is supercritical and buoyant relative to groundwater under typical subsurface conditions. If vertical pathways are available or created through elevated pressure reactivating fractures or faults, CO_2 will tend to flow upward and escape and, depending on geologic conditions, may reach drinking water aquifers or even the land surface (Rinaldi et al., 2014).

Physical testing methods for detecting CO_2 leakage include surface to borehole seismic imaging, cross-well seismic, cross-well electromagnetic, well logs, and tracer injection tests (Benson, 2006). These methods are useful in detecting existing conductive fractures or faults in reservoirs/caprocks (Lee et al., 2012; Luo et al., 2010; Sminchak et al., 2002), but they cannot detect leakage through induced fractures during CO_2 injection and the long-term storage afterwards. A recent study (Zoback et al., 2012) has shown that micro seismic events do not correlate well with "fracturing" in shale gas reservoirs, because slow fault slip does not generate high frequency seismic waves that can be detected by current seismic technology.

Analytical models have also been used to identify CO_2 leakage and specify leakage parameters, such as location, orientation and transmissibility (Sun et al., 2013; Zeidouni, 2012; Zeidouni et al., 2011a,b; Zhou et al., 2008). In these models, pressure buildup or drop tests were carried out to determine the CO_2 and brine displacement in a deep saline aquifer. However, these models were used under simplified conditions, for example, a single injection well and/or single monitoring well in a homogenous reservoir,

* Corresponding author. Tel.: +1 720 278 3875.
E-mail addresses: huangzhqin@upc.edu.cn, huangzhqin@gmail.com (Z.-Q. Huang), rcogfr_upc@126.com (J. Yao).

http://dx.doi.org/10.1016/j.ijggc.2014.12.012
1750-5836/

Nomenclature

A_{ij}	cross area between grid i and j (m^2)
a	coefficient in porosity-stress correlation
b	aperture of fractures (m)
C_i	constants in fractures' permeability–aperture correlation, $i = 1,2$
c	coefficient in permeability–stress correlation
C_R	heat conductivity of rock gains (W/K/m)
d_{ij}	distance between grid i and j (m)
M^κ	accumulation terms of the components κ
$\boldsymbol{F}^\kappa$	flux terms of the components κ along boundaries or cross sections
$\boldsymbol{f}$	body force (Pa/m)
G	shear modulus (Pa)
$\boldsymbol{g}$	gravity acceleration constant (m/s^2)
h	specific enthalpy (J/kg)
$\boldsymbol{I}$	identity matrix
K	bulk modulus (Pa)
K_h	lateral stress coefficient
k	absolute permeability (m^2)
k_0	permeability at zero effective stress (m^2)
k_f	fracture permeability (m^2)
k_{f0}	fracture permeability at zero effective stress (m^2)
k_{rl}	relative permeability of fluid phase l
N_k	numbers of mass components
$\boldsymbol{n}$	the unit normal vector of boundary Γ
p	fluid pressure (Pa)
p_c	capillary pressure (Pa)
p_{c0}	entry capillary pressure (Pa)
p_f	hydraulic fracturing pressure (Pa)
q^κ	sources or sinks terms of the components κ
R	equation residual
S_l	saturation of fluid phase l
T	temperature (K or °C)
T_0	reference temperature (K or °C)
t	time (s)
$\boldsymbol{u}$	displacement vector (m)
V	the domain volume (m^3)
$\boldsymbol{v}$	the Darcy velocity (m/s)
X_l^κ	mass fraction of component κ in fluid phase l

Greek letters

α	Biot's coefficient
β	linear thermal expansion coefficient ($°C^{-1}$)
ϕ	porosity
ϕ_0	porosity at zero effective stress
ϕ_r	porosity at high effective stress
λ	thermal conductivity (W/K/m)
λ_S	Lame's constant (Pa)
ε	strain tensor
ε_v	volumetric strain
ρ	density (kg/m^3)
ν	Poisson's ratio
σ	stress tensor (Pa)
σ_h	horizontal stress (Pa)
σ_m	mean stress (Pa)
σ_v	vertical stress (Pa)
σ'	effective stress (Pa)
σ_R	rock grain density (kg/m^3)
Γ	boundary of domain

Subscripts and superscripts

k	the index for the components
l	fluid phases

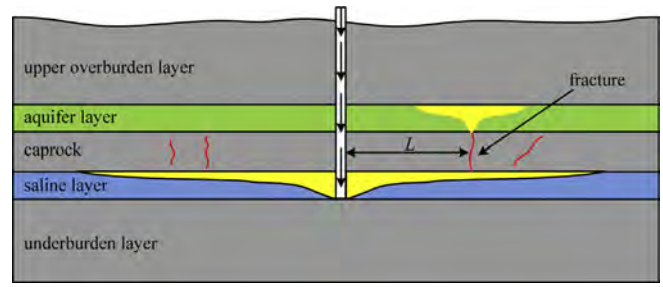

Fig. 1. Schematic of CO_2 injection in the presence of fractures within the caprock layer.

and CO_2 phase properties were simplified as well. The analytical methods have several limitations and they are in general unable to consider the complex phase behavior during CO_2 injection and realistic reservoir heterogeneity.

In comparison, numerical simulations are able to account for CO_2 multiphase flow and complicated phase behavior, diffusion/dispersion, geomechanics (Hu et al., 2013; Winterfeld and Wu, 2012), and chemical reactions (Zhang et al., 2012) during CO_2 injection and storage. So numerical simulation tools are more suitable for quantifying CO_2 leakage locations and rates under realistic field conditions (Pruess and Nordbotten, 2011; Pruess et al., 2003; Rutqvist and Tsang, 2002; Rutqvist et al., 2002; Siriwardane et al., 2013). To predict potential CO_2 leakage pathways and quantify leakage rates in storage geological formations, the effect of geomechanics and rock deformation must be included in the model formulation. This is an active research area and several simulators have been used extensively for CO_2 sequestration modeling, such as the TOUGH2 family of codes (Pruess et al., 1999; Zhang et al., 2008), GEM (Kumar et al., 2008; Siriwardane et al., 2013), DuMux (Class et al., 2009), and OpenGeoSys (Hou et al., 2012).

Physically, CO_2 leakage from a storage formation will occur when the reservoir pressure is high enough to cause mechanical failure in caprocks or in the wellbore (as depicted in Fig. 1). In a CO_2 geological storage reservoir with large storage capacity, the increase in pressure should be gradual and may last for years during continuous CO_2 injection. This is very different from a hydraulic fracturing operation, in which a small-volume packed wellbore section is subject to a high injection rate of fracturing fluid in a very short period of time in order to fracture the rock. Depending on field geological conditions, high pressure buildup in CO_2 storage systems is needed to fracture caprocks or fault zones, and CO_2 is very likely in a liquid or supercritical phase at that high pressure. CO_2 leakage, if occurring, will lead to some drop in pressure that will propagate rapidly in a pressurized, liquid-filled reservoir. The changes in reservoir pressure associated with the occurrence of CO_2 leaking will be "seen" by multiple observation wells equipped with downhole pressure sensors. And the collected data can be analyzed using advanced inverse modeling and optimization schemes to identify leakage that is likely to be occurring. In comparison, the same pressure signals or leakage through fracture zones may not be strong enough to be detected by geophysical or remote sensing technologies.

Therefore, there is a need to understand how the flow and pressure transients are affected by CO_2 multiphase flow and complicated phase behavior, coupled with geomechanical effects. The objectives of this paper are to investigate fluid flow behavior when CO_2 leakage occurs through caprock fractures or geomechanically activated faults by using our parallel fully-implicit and fully-coupled simulator. In this work, we don't focus on explicit modeling of the dynamic propagation of the caprock fractures. Although the fracture propagating process is important to geomechanics and several modeling approaches have been developed

(Lecampion, 2009; Pan et al., 2013; Peirce and Detournay, 2008; Richardson et al., 2011; Xu and Wong, 2010), the fact that numerically simulating the fracture propagation is widely known to be difficult, especially for coupling with large-scale porous flow. Alternatively, we use an implicit, physics-based model to simulate such dynamic process by using several practical correlations (e.g. fracturing pressure functions, porosity/permeability–stress relationships, etc.). The pressure signatures and changes in flow behavior are investigated to explore their use in detecting caprock fractures, which are our concerns.

The paper is organized as follows. We first outline the basic mathematical and numerical models of our simulator, named THM-CO_2, which is a parallel fully-coupled thermal-hydro-mechanical (THM) simulator. Then, the fluid-driven fracture zone is modeled by using a physics-based and practical approach, including the correlations of hydraulic properties. Thereafter, the implement scheme of the codes is explained, and its validity is verified through two analytical solutions. Finally, several CO_2 leakage simulations are conducted in various geomechanical and flow conditions.

2. Mathematical and numerical model

2.1. Multiphase fluid and heat flow model

Our simulator is based on the general mass and energy balance equations (Pruess et al., 1999; Rutqvist et al., 2002; Wu and Qin, 2009). Fluid flow is described by a multiphase extension of Darcy's law and diffusive mass transport is considered in all phases. For the energy balance equation, heat transport occurs by conduction and convection, with sensible as well as latent heat effects included. The description of thermodynamic conditions is based on the assumption of local equilibrium of all phases. Fluid and formation parameters can be arbitrary nonlinear functions of the primary thermodynamic variables. The mass and energy conservation equations in integral form are:

$$\frac{\partial}{\partial t}\int_V M^\kappa \mathrm{d}V = \int_\Gamma \boldsymbol{F}^\kappa \times \boldsymbol{n}\mathrm{d}\Gamma + \int_V q^\kappa \mathrm{d}V \tag{1}$$

The integration is over an arbitrary domain V with closed boundary Γ. Here, M^κ in the accumulation term, with $\kappa = 1, \ldots, N_\kappa$, labeling the mass components (air, water, CO_2, solutes, ...), and $\kappa = N_\kappa + 1$ for the energy "component".

The mass accumulation term is a sum over the fluid phases l (=gas, liquid, NAPL):

$$M^\kappa = \phi \sum_l S_l \rho_l X_l^\kappa \tag{2}$$

The energy accumulation term accounts for fluid phases and rock:

$$M^\kappa = (1-\phi)_{\rho R} C_R T + \phi \sum_l S_l \rho_l \boldsymbol{\upsilon}_l, \quad k = N_k + 1 \tag{3}$$

The mass flux of component κ is a sum over fluid phase l:

$$\boldsymbol{F}^\kappa = \sum_l \rho_l X_l^k \boldsymbol{\upsilon}_l \tag{4}$$

where the Darcy velocity $\boldsymbol{\upsilon}_l$ of phase l is given by the multiphase extension of Darcy's law:

$$\boldsymbol{\upsilon}_l = -k\frac{k_{rl}}{\mu_l}\left(\nabla p_l - \rho_l \boldsymbol{g}\right) \tag{5}$$

For the energy conservation equation, heat flux includes conductive and convective terms:

$$\boldsymbol{F}^\kappa = -\lambda \nabla T + \sum_l \rho_l h_l \boldsymbol{\upsilon}_l, \quad \kappa = N_\kappa + 1 \tag{6}$$

The definitions of all symbols used above can be found in the Nomenclature.

2.2. Geomechanical model

In this work, we fully couple geomechanics to fluid and heat flow. Rock mass is assumed to be a thermal-poroelastic material and obeys a generalized version of Hooke's law (McTigue, 1986):

$$\boldsymbol{\sigma} - \left(\alpha p + 3\beta K\left(T - T_0\right)\right)\boldsymbol{I} = 2G\varepsilon + \lambda_S \varepsilon_V \boldsymbol{I} \tag{7}$$

Relating stresses and displacements are combined to yield an equation for mean stress, which is a function of pore pressure and temperature. The mean stress is an additional primary variable to multiphase flow system. Under the assumption of linear elasticity with small strains for a thermo-poroelastic system, the equations for the stresses in terms of the strains can be expressed as follows (Jaeger et al., 2009). The trace of the general Hooke's law for a thermo-poroelastic medium is:

$$K\varepsilon_V = \sigma_m - \alpha p - 3\beta K\left(T - T_0\right) \tag{8}$$

The additional geomechanical equations, namely the equation of stress equilibrium (momentum):

$$\nabla \cdot \boldsymbol{\sigma} + \boldsymbol{f} = 0 \tag{9}$$

The strain tensor definition $\varepsilon = \left(\nabla \boldsymbol{u} + (\nabla \boldsymbol{u})^T\right)/2$, is combined with Eq. (7) yield to the thermo-poroelastic Navier equation:

$$\nabla\left(\alpha p + 3\beta K\left(T - T_0\right)\right) + (\lambda_S + G)\nabla(\nabla \cdot \boldsymbol{u}) + G\nabla^2 \boldsymbol{u} + \boldsymbol{f} = 0 \tag{10}$$

Taking the divergence of Eq. (10), and combining with Eq. (8) yields the governing equation for mean stress:

$$\frac{3(1-\nu)}{1+\nu}\nabla^2 \sigma_m + \nabla \cdot \boldsymbol{f} - \frac{2(1-2\nu)}{1+\nu}\left(\alpha \nabla^2 p + 3\beta K \nabla^2 T\right) = 0 \tag{11}$$

Note that the divergence of the displacement vector is the volumetric strain. In this paper, only fully elastic problem is considered. Furthermore, the boundary conditions for Eq. (11) are mean stress specified on the boundary, which will be described in Section 2.3.

2.3. Numerical discretization and implementation

In THM-CO_2 simulator, the mass, energy, and momentum balance equations are discretized in space using the integral finite-difference method (Pruess et al., 1999; Wu and Qin, 2009). The simulation domain is subdivided into a structured or unstructured mesh. Time derivatives are evaluated using the standard first-order approximation, and flux and accumulation terms are evaluated fully implicitly. As a result, the set of coupled nonlinear mass and energy conservation equations can be written in residual form as:

$$R_i^\kappa\left(\boldsymbol{x}^{t+\Delta t}\right) = M_i^\kappa\left(\boldsymbol{x}^{t+\Delta t}\right) - M_i^\kappa\left(\boldsymbol{x}^t\right) - \frac{\Delta t}{V_i}\left(\sum_j A_{ij} F_{ij}^\kappa\left(\boldsymbol{x}^{t+\Delta t}\right) + V_i q_i^{\kappa, t+\Delta t}\right) = 0 \tag{12}$$

Similar to the mass and energy equations, the finite difference approximation for Eq. (11) in residual form is (Winterfeld and Wu, 2014):

$$R_i^\kappa\left(\boldsymbol{x}^{t+\Delta t}\right) = \sum_j \left(\frac{3(1-\nu)}{1+\nu}\frac{\sigma_{mj} - \sigma_{mi}}{d_{ij}} - \frac{2\alpha(1-2\nu)}{1+\nu}\frac{p_j - p_i}{d_{ij}} - \frac{2\beta E}{1+\nu}\frac{T_j - T_i}{d_{ij}} + \boldsymbol{f} \cdot \boldsymbol{n}\right)_{ij} A_{ij} = 0 \tag{13}$$

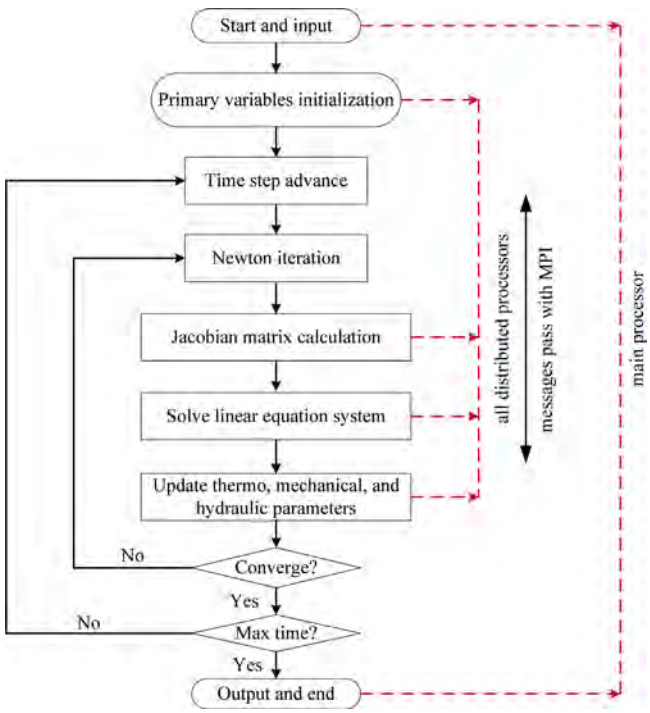

Fig. 2. Numerical implement architecture and flow chat.

Here, $\kappa = N_\kappa + 2$ represents the stress "component".

Strictly speaking, grid block geometry is no longer fixed due to geomechanical effects. However, under the assumption of small deformations, we can neglect this geometrical variation. This is practical for accuracy required for field cases.

The model solves for four primary variables (pressure, air mass fraction/gas saturation, temperature, and mean stress) for each grid block. The primary variables pressure, air mass fraction/gas saturation and temperature are aligned with the mass and energy conservation Eq. (12). Mean stress is aligned with Eq. (13). These equations are solved by the Newton–Raphson method, Eq. (14), which iterates until the residuals are reduced below preset convergence criteria:

$$-\sum_i \frac{\partial R_i^\kappa\left(\boldsymbol{x}^{t+\Delta t}\right)}{\partial x_i}\bigg|_n (\boldsymbol{x}_{n+1} - \boldsymbol{x}_n) = R_i^\kappa\left(\boldsymbol{x}_n^{t+\Delta t}\right) \tag{14}$$

where n denotes the iterative step during one time step. THM-CO_2 is implemented in parallel code and with MPI used for communications between processors. A flow chart for the code is shown in Fig. 2. All data input and output are carried out through the master processor. The most time-consuming computations (assembling the Jacobian matrix, updating thermo physical parameters, and solving linear equation systems) are distributed to all processors (Winterfeld and Wu, 2014).

In the THM-CO2 code, domains are partitioned using the METIS and ParMETIS packages (Karypis and Kumar, 1998a,b) with three partitioning algorithm options, K-Way, VK-Way, and Recursive. Each processor computes Jacobian matrix elements for its own grid blocks. Exchange of information between processors uses MPI (message passing interface) and allows calculation of Jacobian matrix elements associated with inter-block connections across domain partition boundaries. The Jacobian matrix is solved in parallel using an iterative linear solver from the Aztec package (Tuminaro et al., 1999). Aztec solver options include conjugate gradient and generalized minimum residual, among others. The detailed descriptions of the parallel scheme can be found in our previous works (Wang. et al., 2014; Winterfeld and Wu, 2014).

3. Fluid-driven fracture modeling

Caprock acts as a sealing agent with regard to carbon dioxide storage and any fracturing in it may lead to CO_2 leakage from the saline aquifer. There are usually some dormant faults or micro fractures (such as joints) in shale caprock, which will be activated or hydraulic fractured due to the buildup of fluid pressure during the CO_2 injection. Recently, Gor et al. (2013) developed an analytical model to predict fluid-driven fracture propagation, and applied the model to the Krechba aquifer in Salah, Algeria (Rutqvist et al., 2010). Their results show that initially the fracture propagation is very fast: 100 m within less than a minute after initiation. Therefore, we will model such a fracturing process by using a physics-based, practical method rather than explicitly simulating of fracture propagation.

There are two steps in our method. In the first step, an empirical criterion will be used to predict the fracturing pressure, which determines whether the fractures are activated or initialized in grid blocks. In the second, the hydraulic properties, such as porosity and permeability, of these fracturing grid blocks are calculated using stress-dependent correlations.

3.1. Fracturing pressure

There is much experimental and analytical research has been conducted in the past several decades for determining the fracturing pressure. Ghanbari and Shams Rad (2013) summarized the published fracturing equations and developed a new empirical criterion. They compare various published equations, which are listed in Table 1. In this work, the equation developed by Ghanbari and Shams Rad (2013) is used.

In our fully-coupled simulator, only the mean stress and the volume strain are calculated. So, an additional relationship is needed to evaluate the horizontal stress σ_h. For the in-situ state of stress in the subsurface, the vertical stress and horizontal stress are usually related by the lateral stress coefficient K_h, i.e. $\sigma_h = K_h\sigma_v$ (Jaeger et al., 2009). Because the fluid pressure slowly increases during the CO_2 injection period, fluid has time to diffuse into the rock and consequently the rock deforms slowly and uniformly. Therefore, the variation of the lateral stress coefficient would be small, so we assume it is constant. Based on this, we obtain the horizontal confining stress as:

$$\sigma_h = \frac{3K_h}{2K_h + 1}\sigma_m, \quad K_h \in (0, 1) \tag{15}$$

3.2. Correlations of hydraulic properties

In the second step, the hydromechanical rock properties are represented by porosity-stress and permeability–stress relationships. For grid blocks without hydraulic fractures, the matrix porosity, ϕ, is related to the mean effective stress as (Rutqvist and Tsang, 2002):

$$\phi = \phi_r + (\phi_0 - \phi_r)\exp\left(a\sigma'_m\right) \tag{16}$$

And the corresponding permeability is correlated to the porosity according to the following exponential function (Rutqvist and Tsang, 2002):

$$k = k_0 \exp\left(c\frac{\phi}{\phi_0 - 1}\right) \tag{17}$$

Table 1
The summary of the hydraulic fracturing pressure equations.

The researchers	The equations*	m	n/pm
Jaworski et al. (1981)	$p_f = m\sigma_h + \sigma_{ta}$	–	–
Fukushima (1986)	$p_f = \sigma_{min} + q_u$	–	–
Mori and Tamura (1987)	$p_f = m\sigma_c$	1.3–1.6	–
Panah and Yanagisawa (1989)	$p_f = (m\sigma_3 - n\sigma_3)(1 + \sin(\phi_u)) + C_u \cos(\phi_u)$	1.5	0.5
Satoh and Yamaguchi (2008)	$p_f = (m\sigma_3 + p_m)$	1.18–1.82	−14–34 (kPa)
Ghanbari and Shams Rad (2013)	$p_f = m\sigma_h + pm$	1–1.2	20–40 (kPa)

* Please see the definitions of coefficients in corresponding literatures.

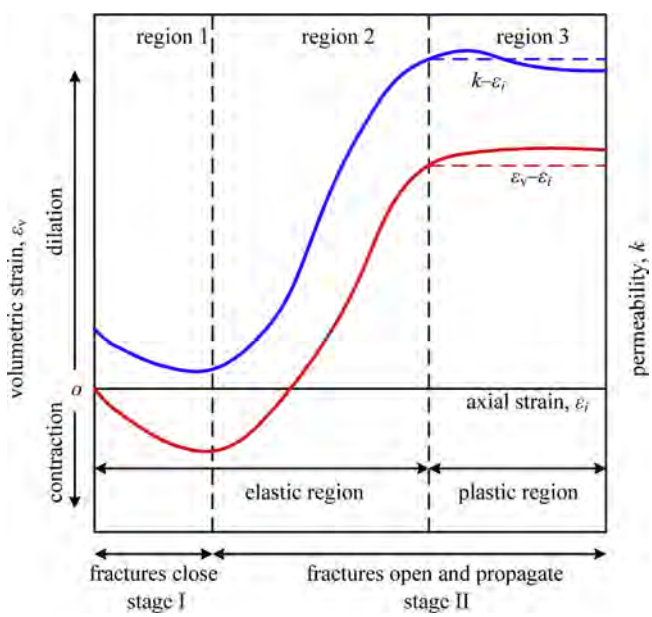

Fig. 3. Schematic relationships among axial strain ε_i, volumetric strain ε_v and permeability k for fractured rock, and the subscript i denotes the ith-direction. (For interpretation of the references to color in this figure legend, the reader is referred to the web version of this article.)

In addition, permeability and porosity are used to scale capillary pressure:

$$p_c = p_{c0}\frac{\sqrt{\phi_0/k_0}}{\sqrt{\phi/k}} \tag{18}$$

For fractured grid blocks, little work has been done to correlate porosity/permeability to stress/strain. Although the stress–strain relationships and rock failure mechanisms have been investigated by many researchers (Heiland, 2003; Martin and Chandler, 1994; Shiping et al., 1994; Zhu and Wong, 1997), little attention has been paid to the permeability–stress or strain relationships of fractured rocks. Based on experimental data, Zhang et al. (2007) have reported that the changes of permeability and volumetric strain follow a similar trend shown in Fig. 3, which agrees with the work of Schulze et al. (2001).

Fig. 3 shows that the behavior of permeability and volumetric strain with axial strain ε_i exhibits two different stages. Stage I commences from the origin until the hydraulic fracture pressure level is reached, during which the existing fractures are closed due to the rock contraction, and permeability decreases gradually. Stage II, after the fracturing pressure level is exceeded, corresponds to the initiation of new fractures, which induces a dramatic increase in permeability and volumetric dilation. Meanwhile two different deformation regions are illustrated in Fig. 3, the elastic- and plastic region. The changes of permeability and volumetric strain in the elastic deformation region can also be divided into two different sub regions, sub region 1 and 2. In sub region 1, permeability and volumetric strain are decreasing and in sub region 2, they are increasing. As aforementioned, we assume rock is elastic medium, so we simplify the model and keep permeability and volumetric strain constant in Fig. 3 by the blue and red dash lines.

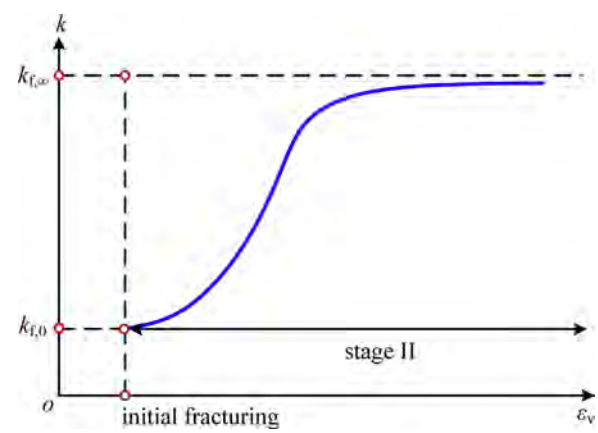

Fig. 4. Schematic relationships between permeability and volumetric strain.

The above indicates that permeability and volumetric strain (or mean stress) are related to each other. In stage I, before fracturing initializing, all the fractures are closed, so the permeability- and porosity–stress correlations are those for matrix, i.e., Eqs. (16) and (17). For stage II, a hypothetical correlation curve is shown in Fig. 4, and can be obtained from lab experiments or field test results. The experimental results of Zhang et al. (2007) also have shown that the cubic dependence of permeability on fracture aperture is valid for a fractured medium and subjected to stresses, so we use the following relationship between permeability and fracture aperture:

$$k_f = k_{f,0}C_1\left(1 + \frac{\Delta b}{C_2}\right)^3 \tag{19}$$

We will use Eq. (19) to evaluate the porosity changes for stage II, because stress-induced changes in hydraulic properties are expected to be much greater in compliant rock fractures than in the stiffer matrix (Rutqvist et al., 2002).

4. Numerical implementation and verification

4.1. 1D Consolidation problem

The consolidation problem, in which a fluid-saturated porous medium is subjected to an instantaneously applied normal load on its upper surface, is one of the most important problems in rock and soil mechanics. Here, a 1D case is simulated and compared to the analytical solution (Jaeger et al., 2009), as depicted in Fig. 5. We simulated this problem in two steps.

In the first step, a load is imposed to produce the pore pressure increase, which is undrained process. We started from an initial state where pore pressures and mean stress were initialized

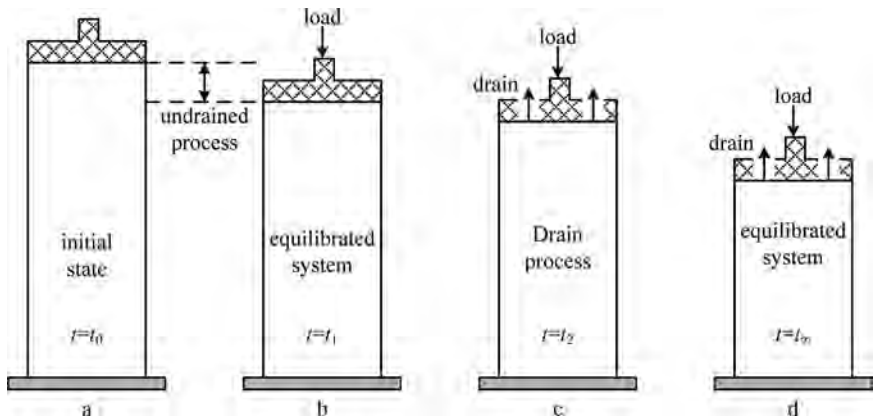

Fig. 5. Schematic of evolution of 1D consolidation problem.

Table 2
Input data for 1D consolidation problem.

Parameters	Value	Unit
Porosity	0.2	–
Permeability	1.0×10^{-13}	m^2
Young's modulus	8.0	GPa
Poisson's ratio	0.2	–
Biot's coefficient	0.2	–
Water compressibility	4.4×10^{-10}	1/Pa
Water viscosity	0.89	mPa·s

at 3.0 MPa and 5.0 MPa, respectively. Then, the additional vertical stress of 3.0 MPa was imposed at the column top that induced a pore pressure increase in the column. In the second step, fluid drainage is simulated. We set the pore pressure at the column top to the initial pore pressure (3.0 MPa). We also set the mean stress at the column top to that calculated from the equilibrated system. Fluid then drained out of the column top as the pore pressure in the column returned to the initial value. The dimensions of the simulated model is 1 m × 1 m × 100 m ($x \times y \times z$), and the grid size is 1 m, 1 m, and 0.25 m in x, y, z directions respectively. The detailed input data is listed in Table 2. The comparison of pore pressure between our numerical simulations and analytical solutions in Fig. 6 indicates that our numerical results produce essentially the same answers to analytical models, which verifies the validity of our numerical model and approach.

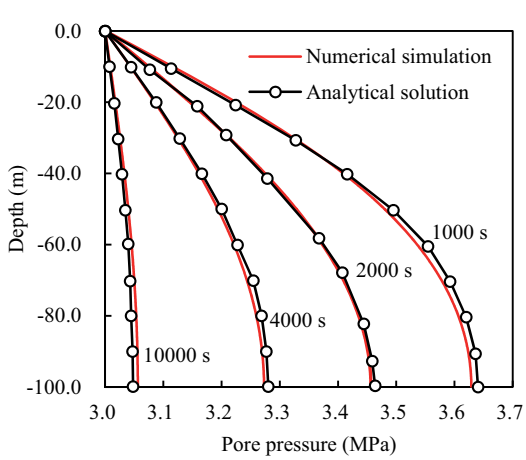

Fig. 6. Comparison of pore pressure between numerical results and analytical solutions.

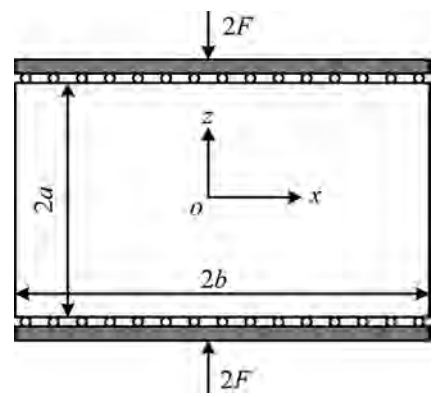

Fig. 7. Schematic of 2D Mandel's problem.

4.2. 2D Mandel's problem

Next, we consider the original two-dimensional Mandel problem, which is depicted as Fig. 7. A constant compressive force is applied to the top and bottom of a water-filled poroelastic material, inducing an instantaneous uniform pore pressure increase and compression. The lateral boundary surfaces perpendicular to the x-direction are at the ambient pressure and are traction free. The pore pressure near the surfaces will decrease due to drainage. The material there becomes less stiff and an additional load will transfer to the center, resulting in a further increase in center pore pressure that reaches a maximum and then declines. This phenomenon is called the Mandel–Cryer effect (Cryer, 1963; Mandel, 1953), and Abousleiman et al. presented an analytical solution to the above problem that we compare our simulated results to Abousleiman et al. (1996).

We simulated the Mandel–Cryer effect problem for a 1000 m square domain that was subdivided into a uniform 200 × 200 grids. The initial pore pressure and mean stress were 0.1 MPa, the applied mean stress was 5.0 MPa, the equilibrium pore pressure was 2.179 MPa. The system drained for 50,000 s. Table 3 gives

Table 3
Rock properties for Mandel problem.

Input parameters	Value	Unit
Porosity	0.094	–
Permeability	1.0×10^{-13}	m^2
Young's modulus	5.0	GPa
Poisson's ratio	0.25	–
Biot's coefficient	1.0	–
Pore compressibility	0	–

Table 4
Rock properties for CO_2 leakage simulation model.

Parameters	Overburden	Aquifer	Caprock	Saline	Underburden
Zero stress porosity, ϕ_0	0.01	0.1	0.01	0.1	0.01
Residual porosity, ϕ_r	0.0904	0.094	0.0094	0.094	0.0094
Zero stress permeability, k (m^2)	4.0×10^{-15}	1.0×10^{-13}	4.0×10^{-19}	1.0×10^{-13}	4.0×10^{-18}
Young's modulus, E (GPa)	5.0	5.0	5.0	5.0	5.0
Poisson's ratio, ν	0.25	0.25	0.25	0.25	0.25
Biot's coefficient, α	1.0	1.0	1.0	1.0	1.0
Saturated rock density, ρ_S $\left(kg/m^3\right)$	2260	2260	2260	2260	2260
Corey's irreducible gas saturation	0.05	0.05	0.05	0.05	0.05
Corey's irreducible liquid saturation	0.3	0.3	0.3	0.3	0.3
van Genuchten function exponent, m	0.457	0.457	0.457	0.457	0.457
Entry capillary pressure, p_{c0} (Pa)	1.96×10^6	1.96×10^5	3.125×10^7	1.96×10^5	3.125×10^7

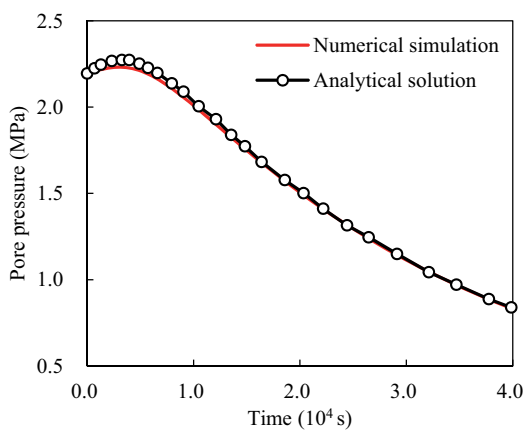

Fig. 8. Pore pressure at the center of domain.

the material properties used in this simulation. Fig. 8 shows the comparison of pressure at the center of the domain between the simulation and the analytical solution. The simulated pressure has a peak and shows excellent agreement with the analytical solution, which lends creditability to our computational approach again.

5. CO_2 leakage simulation and flow behavior analysis

5.1. Fundamental computational model

As shown in Fig. 9, a multi-layered geologic profile is considered in this study with a pre-existing fractured zone or dormant fractures in the caprock, which may be activated during fluid injection. There are five geologic layers: the upper overburden strata, the aquifer layer, the shale caprock, the saline layer where CO_2 injection is planned, and the underburden layer. A vertical injection well is placed in the center of the simulation model at a depth of 1495 m, where the CO_2 is at a temperature and pressure for it to be a supercritical fluid. The material properties for each layers are given in Table 4.

Primary variables are initialized at the start of a simulation. In this study, it is desirable for the simulation initialization to be hydrostatically stable such that if the system were isolated, the primary variables would not change over time. In this hydrostatic stability calculation, the temperature is assumed to be 10 °C on the ground surface and 85 °C at 3000 m depth, resulting in a temperature gradient of 25 °C/km. The pressure at the ground surface is assumed to be atmospheric (0.1 MPa) and, after the steady state calculation, a pressure of 30 MPa is obtained at the bottom of the model. The initial stress is assumed to be isotropic and has a depth gradient corresponding to the acceleration of gravity (9.81 m/s^2) multiplied by the rock density (2260 kg/m^3). The initial porosity and permeability are calculated using the initial stress field and Eqs. (16) and (17). The relative permeability and capillary pressure use Corey's function and van Genuchten's function respectively (Rutqvist and Tsang, 2002).

5.2. Influence of a pre-existing fractured zone

In this section, we show the results of CO_2 injection modeling in the presence of a fractured zone. Based on the results of the hydrostatic calculation, the initial temperature and pressure at the injection point are 47.5 °C and 15 MPa, respectively, and injected CO_2 is a supercritical fluid. Compressed CO_2 is injected at a constant rate of 0.05 kg/s. First, we investigate the influence of a fractured zone in the caprock. A vertical narrow permeable zone with 10 m width was included in the caprock at 300 m from the injection source (i.e. at $x = 4305$ m). The model mesh is constructed with a refined grid in the aquifer, caprock, and saline layers and around well where significant gradients may occur. The x- and z-direction grid block thickness are shown in Table 5.

For simplicity, material properties of the pre-existing fractured zone are those of the saline layer. In the numerical simulation, the grid blocks located on the outer boundaries remain at hydrostatic

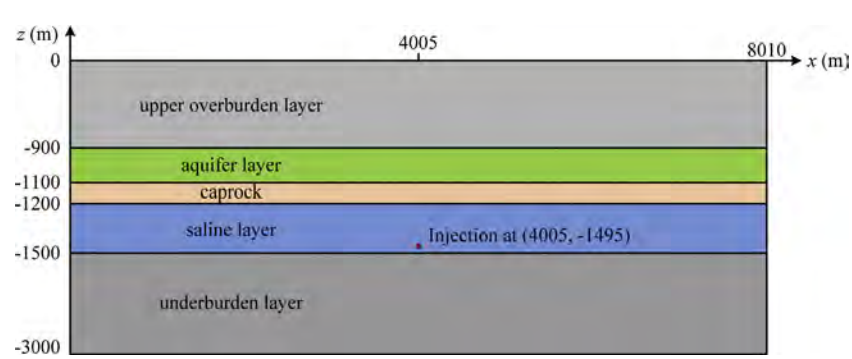

Fig. 9. Geometry model for CO_2 injection simulation.

Table 5
The grid block numbers and thickness.

Direction	Grid numbers and thickness							
x	Numbers	10	10	10	101	10	10	10
	Thickness (m)	200	100	50	10	50	100	200
z	Numbers	10	20	20	10	30	10	26
	Thickness (m)	50	20	10	10	10	20	50

pressure except the bottom boundary. Fig. 10a shows the spread of CO_2 plume in the reservoir with and without the presence of a simulated fractured zone at the end of one year injection period. The difference between their pressure profiles can be found in Fig. 10b, and CO_2 remains as a supercritical fluid in aquifer layer. Fig. 10c shows the volumetric strain caused by the CO_2 injection in the absence and presence of a fractured zone. Although the volumetric strain profiles are changed greatly, computed ground surface deformations computed were relatively smaller. By further considering the heterogeneity of formations, their displacement patterns would be more complicated, and may not be strong enough to be detected by geophysical or remote sensing technologies.

5.3. Modeling of fluid-driven fracturing during CO_2 injection

In this section, we show the results of CO_2 injection modeling in the presence of a potential fluid-driven fracturing zone, which includes dormant fault or micro fractures near the interface between the caprock and saline layers. The initial and boundary conditions are the same as in Section 5.2. To calculate fracturing pressure, we use the coefficient $m = 1.08$, $p_m = 40$ kPa, and the lateral stress coefficient $K_h = 0.3$. A vertical potential hydraulic fracturing zone with 10 m width was included in the caprock at 300 m from the injection source (i.e. at $x = 4305$ m). The model mesh is constructed with a refined grid in the aquifer, caprock, and saline layers, and around well as shown in Table 5. The permeability–stress correlation in Stage II is given as follows based on the model presented by Walsh (1981) and National-Research-Council (US), 1996.

$$k_f = k_{f0}\left(C \ln \frac{\sigma_{f0}}{\sigma_f - p}\right)^3 \tag{20}$$

where k_f is the permeability of hydraulic fractured zone, k_{f0} is the initial permeability of hydraulic fractured zone at Stage II as shown in Fig. 4, σ_f is the normal stress on the fracture zone, σ_{f0} is the reference state at the beginning of Stage II, and C is a constant which is determined by the initial reference state.

First, we investigate the influence of different injection rates on flow behaviors. Compressed CO_2 is injected at four different

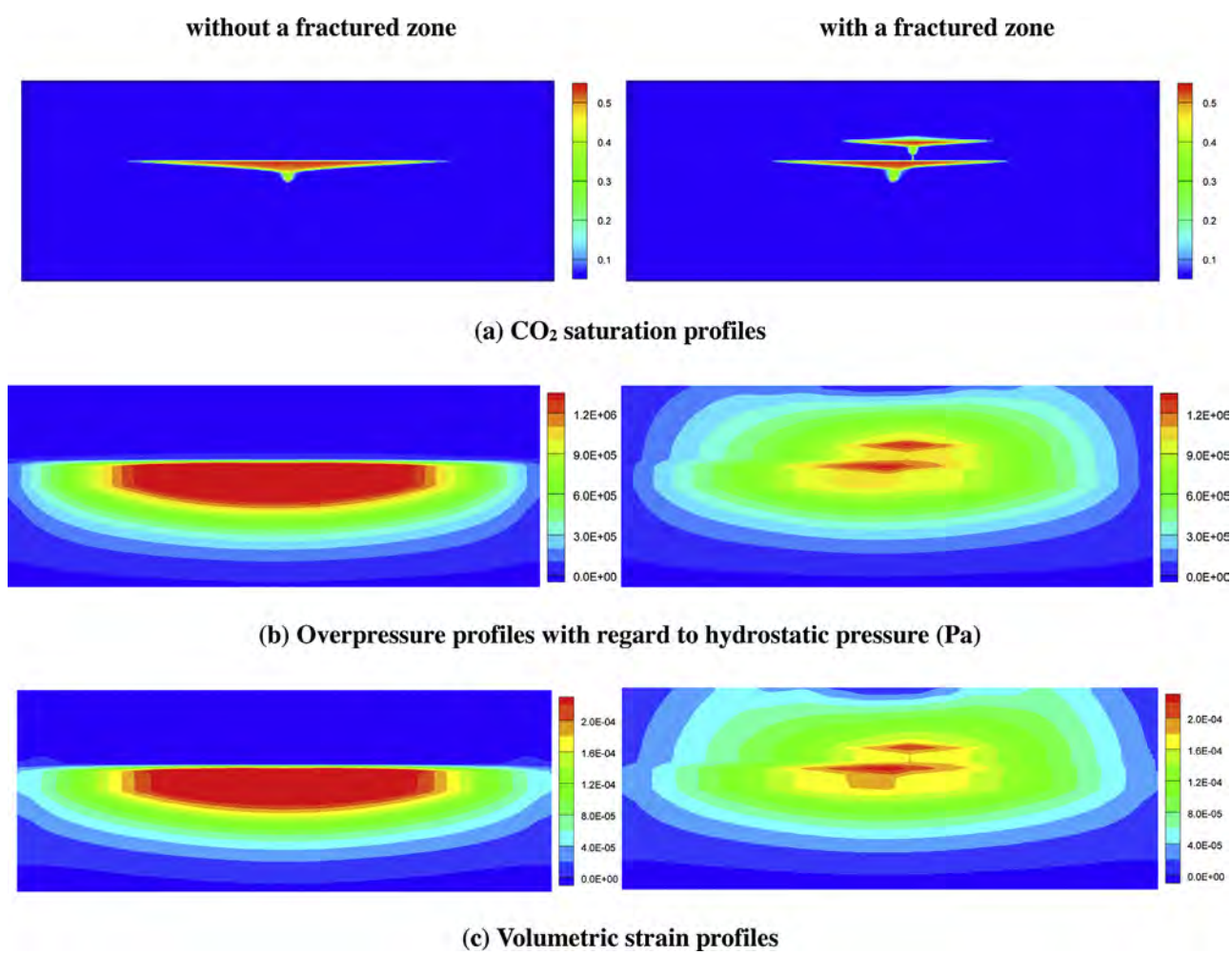

Fig. 10. Comparison of simulation results between computational models in the absence and presence of a fractured zone after 10-years CO_2 injection.

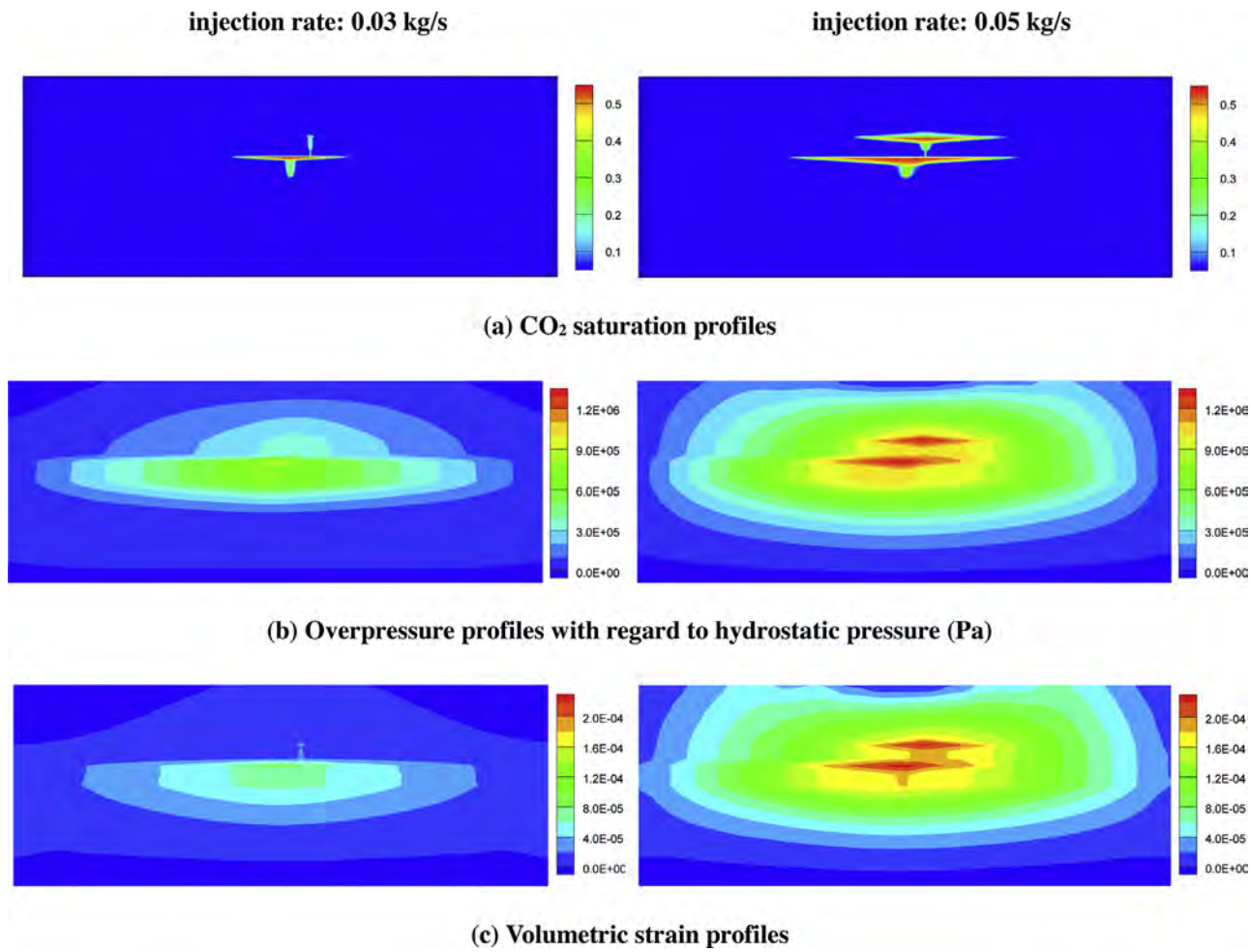

Fig. 11. Comparison of simulation results between different injection rates after 10-years CO_2 injection.

constant rates of 0.01 kg/s, 0.03 kg/s, 0.05 kg/s and 0.07 kg/s. In the numerical simulation, the grid blocks located on the outer boundaries remain at hydrostatic pressure except those on the bottom boundary. Fig. 11 shows the comparison of simulation results between injection rate 0.03 kg/s and injection rate 0.05 kg/s after 10-years CO_2 injection. Here, the initial fracturing permeability $k_{f0} = 0.1$ mD (10^{-13} m^2). All the simulation results are similar to the case with a pre-existing fractured zone.

In order to investigate the influence of the fluid-driven fracture process on the pressure response, we assume that there are two permanent downhole gauges (PDG) for continuous pressure data collection in the aquifer and saline layers. The PDG technology is relatively mature and has been used in the petroleum industry for decades (Horne, 2007). Two gauges are located at positions (4005 m, −905 m) (Monitoring Point 1) and (4005 m, −1495 m) (Monitoring Point 2), respectively.

Fig. 12 shows the comparison of pressure increase at the Monitoring Point 1 in the aquifer layer between different modeling scenarios. For the modeling scenario without any fractured zones, the pressure changes are small and the maximum changes is 35 kPa. However, the pressure increases in the initial stage and then decreases to the hydrostatic pressure. This can be explained by the Mandel–Cryer effect due to consolidation, which has discussed in Section 4.2. For the modeling scenario with a pre-existing fractured zone, the pore pressure increases gradually from the beginning of CO_2 injections. Although a similar phenomenon can be found in the modeling scenario with a hydraulic fracturing zone, a distinct change in the pressure signature can be seen in Fig. 12. Before the zone was fractured or activated, the corresponding pressure response should be same as the case without any fractures. In this case, the initial hydraulic fracturing took place after 102 days. This enable us to identify an existing fractured zone which may be activated or newly created.

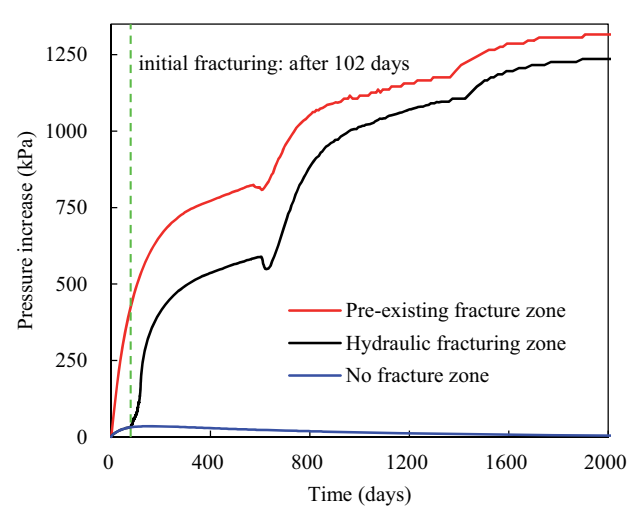

Fig. 12. Pressure changes in the Monitoring Point 1 with different modeling scenarios and injection rate 0.05 kg/s.

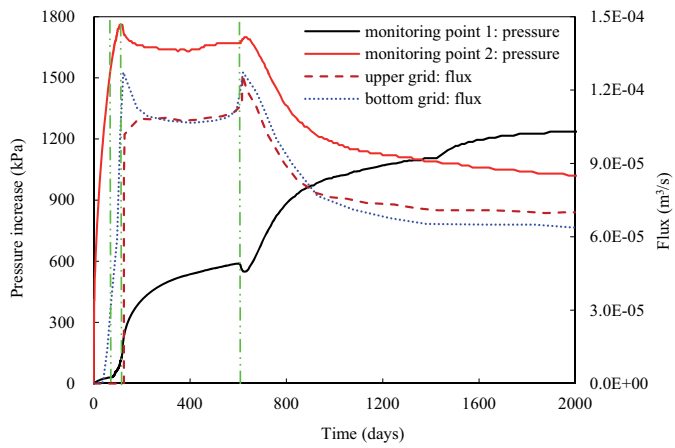

Fig. 13. The pore pressure changes at the monitoring points and fluxes changes of the upper and bottom grids in the fluid-driven fracturing zone during CO_2 injection.

As shown in Fig. 13, a strong correlation between the leakage fluxes from the fractured zone and pore pressures at Monitoring Points can also be observed. At the beginning, the permeability of the fluid-driven fracturing zone is the same as that of the surrounding caprock grid blocks due to the closure of the micro fractures and dormant faults. With the pore pressure increasing during CO_2 injection, the effective stress is reduced in fractured zone and consequently, the fractures tends to open. In this stage, the pressure at Monitoring Point 2 increases straightly till the entire fractured zone are fractured. When the fractured zone begins to leakage, a sudden pressure drop at Monitoring Point 2 is observed because of the connection between the saline layer and aquifer layer. Meanwhile, the fluxes will also decrease with the drop of pressure because the effective stress increases.

In addition, there is a sudden pressure drop in the pressure curves at Monitoring Point 1, as shown in Figs. 12 and 13. This peculiar phenomenon is the signal of CO_2 infusion into fractured zones, as shown in Fig. 14. The beginning of pressure drop indicates that supercritical CO_2 is starting to invade the fractured zone. When the CO_2 fully penetrates the caprock along the fractured zone, the pressure increases again as shown in Fig. 14b. There are several contributing factors: (1) the relative permeability for CO_2 fluid flow increases as the entire fractured zone are saturated with CO_2; (2) supercritical CO_2 is much less viscous than the brine and water, and its mobility increases when fractured zone is saturated with CO_2; (3) when CO_2 fully penetrate the fractured zone, the high-pressure layer and low-pressure layer are communicated with each other, and this result in the pressure drop in the fractured zone.

Fig. 15 shows the influence of different injection rates on the pressure changes. Results show similar trends for different injection rates except for the relative lower rate 0.01 kg/s. Fluid-driven fracturing will not take place with such relative lower injection rate (the blue line). From the simulation results, the times of initial fracturing with different injection rates are 74 days, 102 days, and 210 days, respectively. In addition, the pressure increases shown in Fig. 15 are different for different injection rates.

5.4. Influence of different parameters of fractured zones

In this section, we will further investigate the influence of different parameters for hydraulic fractured zones on the pressure response, including the initial hydraulic fracturing permeability, the location, and the amount of fractured zones. For simplicity, all the model properties in the following numerical simulations are same as the simulations in Section 5.3. Here, the injection

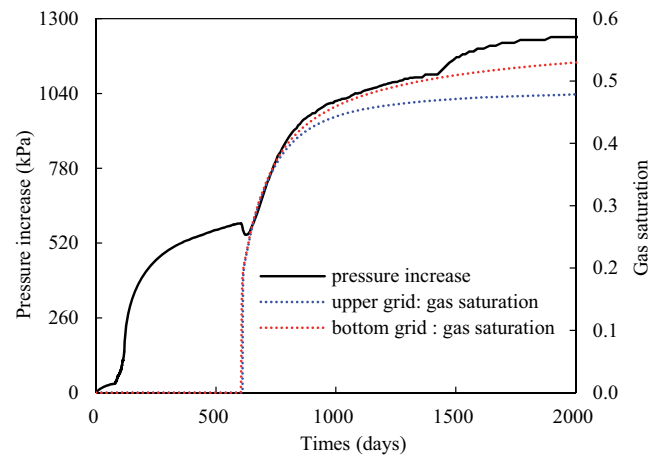

(a) the changes of pressure and saturation during CO2 injection

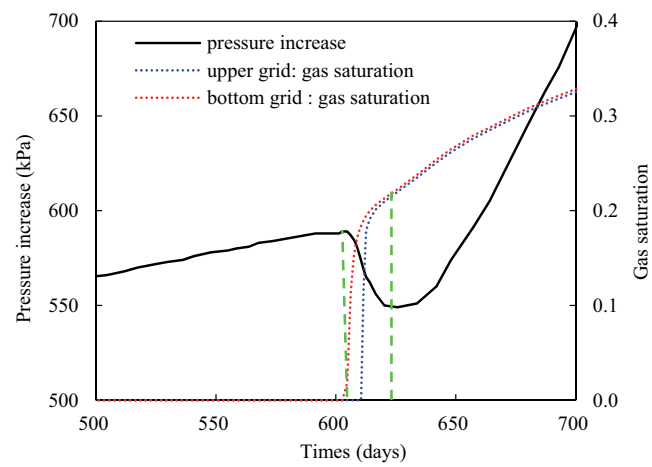

(b) local magnification of the pressure drop stage

Fig. 14. The pore pressure changes at the Monitoring Point 1 and gas saturation changes of the upper and bottom grids in the hydraulic fracturing zone during CO_2 injection.

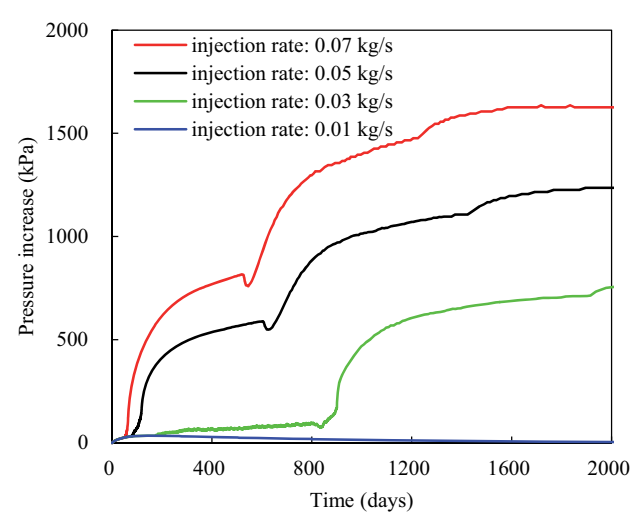

Fig. 15. Pressure changes in the Monitoring Point 1 with different injection rates.

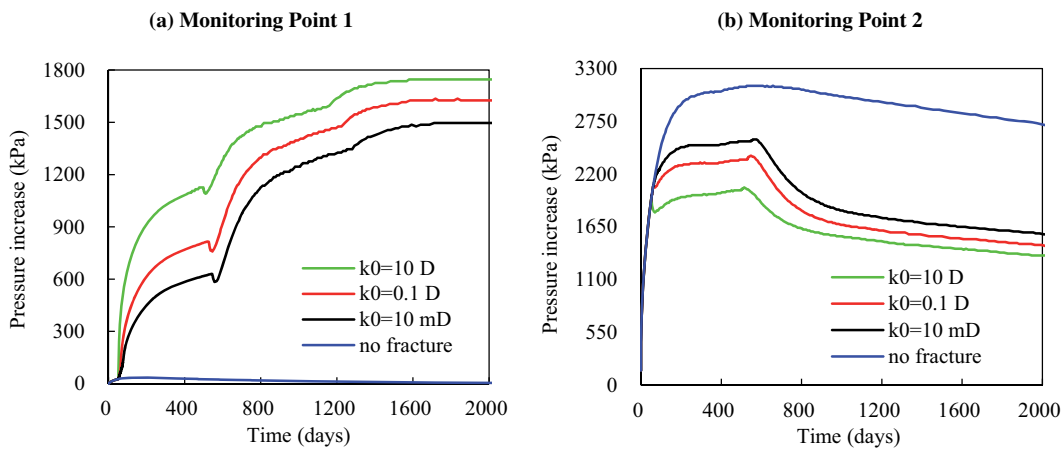

Fig. 16. Pore pressure changes at the monitoring points with different initial hydraulic fracturing permeabilities. (For interpretation of the references to color in this figure legend, the reader is referred to the web version of this article.)

rate is constant, i.e. 0.07 kg/s, and the fractured zone is located at $x = 4305$ m.

(1) Influence of initial fracture permeability

Fig. 16 shows the influence of initial fracture permeability on pressure changes. Although the initial hydraulic fracturing permeability differs, the initial fracturing time is the same. For Monitoring Point 1, the results show the similar trends for pressure changes using different injection rates (as depicted in Fig. 14). However, there are some differences for Monitoring Point 2. In principle, the magnitude of pressure increase trends to decrease with increasing in initial fracture permeability.

As shown in Fig. 16b, there are three distinct stages for these pressure changes. In Stage 1, before fracturing, the pressure down hole increases quickly due to the CO_2 injection. In this stage, CO_2 displaces the saline and transports to the upper layer, the pore pressure increases noticeably in a short time. When the fluid-driven fracturing occurs, in the Stage 2, the pressure increases relative slowly. After CO_2 fully penetrates the caprock, Stage 3 starts and pressure decreases gradually. Moreover, for a relative larger permeability ($k_{f0} = 10$ D), the pressure may decrease suddenly when fluid-driven fracturing begins, as shown in Fig. 16b (green line). These characteristics can be helpful to identify the fracturing of caprocks.

(2) Influence of the location of a fractured zone

The current study also investigates the influence of fracture locations on the pressure response. Three scenarios of a fractured zone with different distances away from the injection source have been run. Fig. 17 shows the pressure responses at two Monitoring Points.

It is observed that the farther the fractured zone is from the injection source, the smaller the magnitude of pressure signals are reduced. Therefore, the variation in pore pressure response at the monitoring points could be helpful to determine the location of fracture zones in the caprock. Meanwhile, we can find that the initial fracturing times are little different between different locations. However, the time of CO_2 fluid arrived at fracture zones are very different. This is because the transient pressure transient transmit more quickly than the mass components. So it is better to use a pressure signal other than a fluid phase monitor to identify the existence of fractures in the caprock.

(3) Influence of the distribution of fractured zones

In order to investigate the influence of the numbers of fracture zones, three scenarios are run in this section. The first scenario only includes one fracture zone which locates at $x = 4105$ m. The second scenario contains two fracture zones which are at $x = 4105$ m and 4305 m, respectively. The third scenario contains three fracture zones which are at $x = 4105$ m, 4305 m, and 4505 m, respectively. And the properties of these fracture zones are same as the example in Section 5.3.

Fig. 18 shows the pressure response at two Monitoring Points. It was observed that the initial fracturing times are the same and the times of CO_2 fluid invaded into fracture zones are also the same. This is because the pressure signal is dependent on the closer

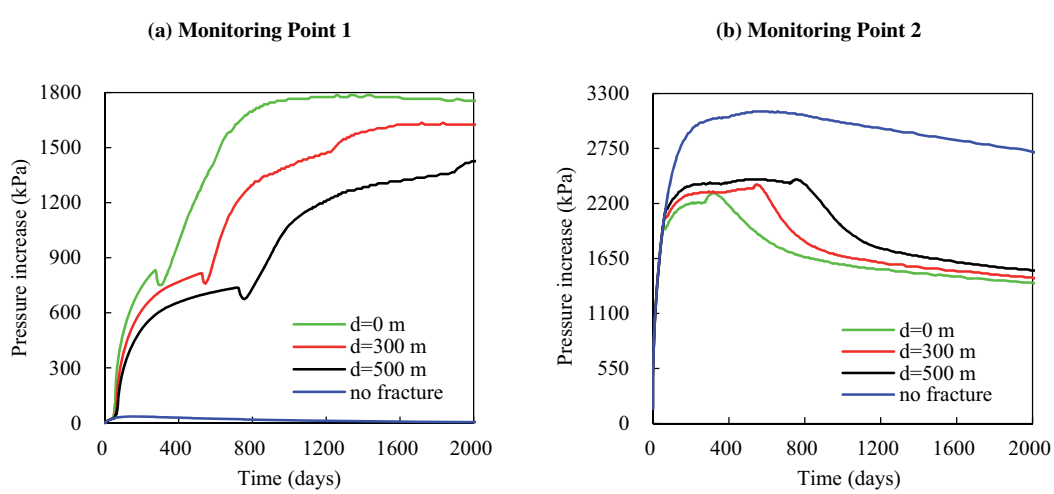

Fig. 17. Pore pressure changes at the monitoring points with different distances away from injection source.

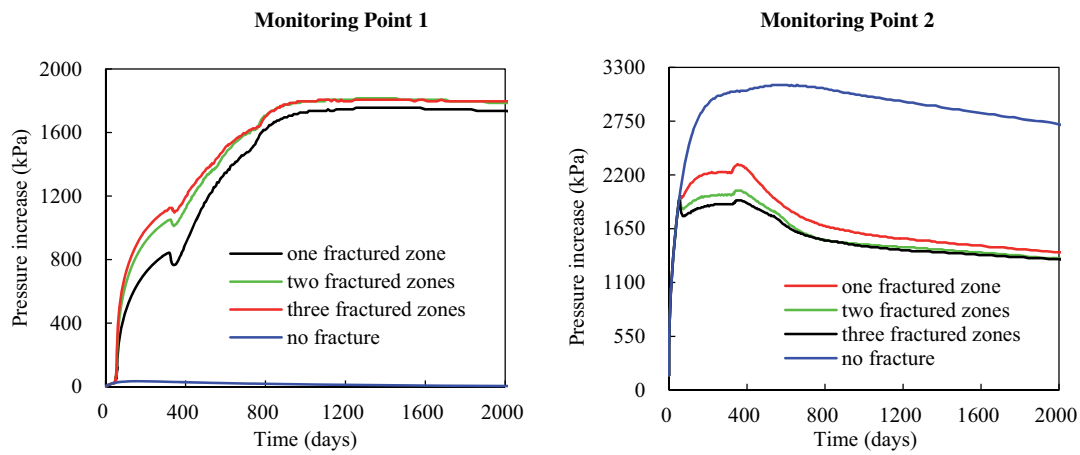

Fig. 18. Pore pressure changes at the monitoring points with different numbers of fractured zones.

fracture zone. With the increase in numbers, the pressure increase curves are more coincident, and the magnitudes of pressure signal are increased at Monitoring Point 2. The opposite phenomena can be found at Monitoring Point 1.

6. Conclusions

In this work, an efficient parallel fully-implicit simulator, named THM-CO_2, has been developed to couple thermal, hydraulic and mechanical (THM) processes in geological media for CO_2 storage. The validity of the numerical model is verified by comparison of numerical results with the analytical solutions of two classical consolidation problems. Based on THM-CO_2, a set of numerical experiments have been run to investigate the fluid flow behavior during CO_2 injection, especially for CO_2 leakage through geomechanically caprock fractures or activated faults. In this paper, we propose an implicit and simplified model to simulate the fracture propagation by using some practical correlations (e.g. hydraulic fracturing pressure functions, permeability–stress relationships, etc.) rather than explicit simulation. The main conclusions drawn from this study are as follows:

(1) If a vertical pathway is available or created due to the pressure buildup during CO_2 injection, CO_2 tends to flow upward and escape, and may reach to the upper aquifer layer. The simulation results indicate that the transient pressure response can be detected by using permanent downhole gauges (PDGs). Meanwhile, the results show that there are strong correlations between the monitoring pressures and CO_2 leakage flux from the fractured zone. At the beginning of fluid-driven fracturing, the pressure of PDGs in aquifer layer will increase suddenly, and the pressure increase trend will slow down or suddenly drop with continual injection. These transient pressure signals enable us to identify the existence of fractures in caprock.
(2) The injection rate is the major factor for fluid-driven fracturing in caprock. It is directly determine the initial fracturing time. The simulation results suggested that slowly increasing the injection rate at the beginning of CO_2 injection may reduce possibility of caprock damage. There should be a critical injection rate to fracture caprock. In this study, the critical injection rate is between 0.01 kg/s and 0.015 kg/s.
(3) The numerical results show that similar trends of pressure increase at PDGs are found with different parameters of fractured zone, such as location, initial fracture permeability and the amount of fractured zones. Specifically, these indicate that it is possible to develop a technical approach by integrating in-situ pressure data, measured from PDGs of multiple wells, into modeling analysis using the THM-CO_2 simulator developed for CO_2 storage in reservoirs, to quantify the potential leakage pathways as well as leaking rates.

Acknowledgements

This work was supported by the CMG Foundation, the National Natural Science Foundation of China (Grant nos. 51404292, 51234007), Natural Science Foundation of Shandong Province of China (ZR2014EEQ010), and the Fundamental Research Funds for the Central Universities of China (13CX05007A, 13CX02052A, 14CX05027A, 14CX06091A).

References

Abousleiman, Y., Cheng, A.-D., Cui, L., Detournay, E., Roegiers, J.-C., 1996. 'Mandel's problem revisited. Geotechnique 46 (2), 187–195.
Benson, S.M., 2006. Monitoring carbon dioxide sequestration in deep geological formations for inventory verification and carbon credits. In: SPE Annual Technical Conference and Exhibition, Society of Petroleum Engineers.
Bolster, D., 2014. The fluid mechanics of dissolution trapping in geologic storage of CO_2. J. Fluid Mech. 740, 1–4, http://dx.doi.org/10.1017/jfm.2013.531.
Class, H., Ebigbo, A., Helmig, R., Dahle, H.K., Nordbotten, J.M., Celia, M.A., Audigane, P., Darcis, M., Ennis-King, J., Fan, Y., et al., 2009. A benchmark study on problems related to CO_2 storage in geologic formations. Comput. Geosci. 13 (4), 409–434.
Cryer, C., 1963. A comparison of the three-dimensional consolidation theories of biot and terzaghi. Q. J. Mech. Appl. Math. 16 (4), 401–412.
Fukushima, S., 1986. Hydraulic fracturing criterion in the core of fill dams. Rep. Fujita Kogyo Tech. Inst. 22, 131–136.
Ghanbari, A., Shams Rad, S., 2013. Development of an empirical criterion for predicting the hydraulic fracturing in the core of earth dams. Acta Geotech., 1–12, http://dx.doi.org/10.1007/s11440-013-0263-2.
Gor, G.Y., Stone, H.A., Prevost, J.H., 2013. Fracture propagation driven by fluid outflow from a low-permeability aquifer. Transport Porous Med. 100 (1), 69–82, http://dx.doi.org/10.1007/s11242-013-0205-3.
Heiland, J., 2003. Laboratory testing of coupled hydro-mechanical processes during rock deformation. Hydrogeol. J. 11 (1), 122–141.
Horne, R.N., 2007. Listening to the reservoir—interpreting data from permanent downhole gauges. J. Pet. Technol. 59 (12), 78–86.
Hou, Z., Gou, Y., Taron, J., Gorke, U.J., Kolditz, O., 2012. Thermo-hydro-mechanical modeling of carbon dioxide injection for enhanced gas-recovery (CO_2-egr): a benchmarking study for code comparison. Environ. Earth Sci. 67 (2), 549–561.
Hu, L., Winterfeld, P.H., Fakcharoenphol, P., Wu, Y.-S., 2013. A novel fully-coupled flow and geomechanics model in enhanced geothermal reservoirs. J. Pet. Sci. Eng. 107, 1–11.
Huppert, H.E., Neufeld, J.A., 2014. The fluid mechanics of carbon dioxide sequestration. Annu. Rev. Fluid Mech. 46, 255–272.
Jaeger, J.C., Cook, N.G., Zimmerman, R., 2009. Fundamentals of Rock Mechanics. John Wiley & Sons, Malden, MA, USA.
Jaworski, G.W., Duncan, J.M., Seed, H.B., 1981. Laboratory study of hydraulic fracturing. J. Geotech. Geoenviron. Eng. 107, 713–732 (ASCE 16287 Proceeding).
Karypis, G., Kumar, V., 1998a. A fast and high quality multilevel scheme for partitioning irregular graphs. SIAM J. Sci. Comput. 20 (1), 359–392.
Karypis, G., Kumar, V., 1998b. A parallel algorithm for multilevel graph partitioning and sparse matrix ordering. J. Parallel Distrib. Comput. 48 (1), 71–95.

Kumar, A., Datta-Gupta, A., Shekhar, R., Gibson, R., 2008. Modeling time lapse seismic monitoring of CO_2 sequestration in hydrocarbon reservoirs including compositional and geochemical effects. Pet. Sci. Technol. 26 (7–8), 887–911.
Lecampion, B., 2009. An extended finite element method for hydraulic fracture problems. Commun. Numer. Methods Eng. 25 (2), 121–133.
Lee, J., Min, K.-B., Rutqvist, J., et al.,2012. Evaluation of leakage potential considering fractures in the caprock for sequestration of CO_2 in geological media. In: 46th US Rock Mechanics/Geomechanics Symposium. American Rock Mechanics Association.
Luo, Z., Bryant, S.L., et al., 2010. Influence of thermo-elastic stress on CO_2 injection induced fractures during storage. In: SPE International Conference on CO_2 Capture Storage and Utilization\, Society of Petroleum Engineers.
Mandel, J., 1953. Consolidation des sols (étude mathématique). Geotechnique 3 (7), 287–299.
Martin, C., Chandler, N., 1994. The progressive fracture of lac du bonnet granite. Int. J. Rock Mech. Min. Sci. Geomech. Geoeng. Abstr. 31, 643–659 (Elsevier).
McTigue, D., 1986. Thermoelastic response of fluid-saturated porous rock. J. Geophys. Res.: Solid Earth (1978–2012) 91 (B9), 9533–9542.
Mori, A., Tamura, M., 1987. Hydrofracturing pressure of cohesive soils. Soils Found. 27 (1), 14–22.
National-Research-Council (US), 1996. Rock Fractures and Fluid Flow: Contemporary Understanding and Applications. National-Research-Council (US), Washington, D.C.
Pan, P.-Z., Rutqvist, J., Feng, X.-T., Yan, F., 2013. Modeling of caprock discontinuous fracturing during CO_2 injection into a deep brine aquifer. Int. J. Greenhouse Gas Control 19, 559–575.
Panah, A.K., Yanagisawa, E., 1989. Laboratory studies on hydraulic fracturing criteria in soil. Soils Found. 29 (4), 14–22.
Peirce, A., Detournay, E., 2008. An implicit level set method for modeling hydraulically driven fractures. Comput. Meth. Appl. Mech. Eng. 197 (33), 2858–2885.
Pruess, K., Nordbotten, J., 2011. Numerical simulation studies of the long-term evolution of a CO_2 plume in a saline aquifer with a sloping caprock. Transport Porous Med. 90 (1), 135–151.
Pruess, K., Oldenburg, C., Moridis, G., 1999. Tough2 User's Guide Version 2. Lawrence Berkeley National Laboratory.
Pruess, K., Xu, T., Apps, J., Garcia, J., et al., 2003. Numerical modeling of aquifer disposal of CO_2. SPE J. 8 (01), 49–60.
Richardson, C.L., Hegemann, J., Sifakis, E., Hellrung, J., Teran, J.M., 2011. An xfem method for modeling geometrically elaborate crack propagation in brittle materials. Int. J. Numer. Methods Eng. 88 (10), 1042–1065.
Rinaldi, A.P., Rutqvist, J., Cappa, F., 2014. Geomechanical effects on CO_2 leakage through fault zones during large-scale underground injection. Int. J. Greenhouse Gas Control 20, 117–131.
Rutqvist, J., Tsang, C.-F., 2002. A study of caprock hydromechanical changes associated with CO_2-injection into a brine formation. Environ. Geol. 42 (2–3), 296–305.
Rutqvist, J., Vasco, D.W., Myer, L., 2010. Coupled reservoir-geomechanical analysis of CO_2 injection and ground deformations at in Salah, Algeria. Int. J. Greenhouse Gas Control 4 (2), 225–230.
Rutqvist, J., Wu, Y.-S., Tsang, C.-F., Bodvarsson, G., 2002. A modeling approach for analysis of coupled multiphase fluid flow, heat transfer, and deformation in fractured porous rock. Int. J. Rock Mech. Min. Sci. 39 (4), 429–442.
Satoh, H., Yamaguchi, Y., 2008. Laboratory hydraulic fracturing tests for core materials using large size hollow cylindrical specimens. In: The First International Symposium on Rockfill Dams, Chengdu, China.
Schulze, O., Popp, T., Kern, H., 2001. Development of damage and permeability in deforming rock salt. Eng. Geol. 61 (2), 163–180.
Shiping, L., Yushou, L., Yi, L., Zhenye, W., Gang, Z., 1994. Permeability-strain equations corresponding to the complete stress—strain path of yinzhuang sandstone. Int. J. Rock Mech. Min. Sci. Geomech. Abstr. 31 (4), 383–391.
Siriwardane, H.J., Gondle, R.K., Bromhal, G.S., 2013. Coupled flow and deformation modeling of carbon dioxide migration in the presence of a caprock fracture during injection. Energy Fuels 27 (8), 4232–4243.
Sminchak, J., Gupta, N., Byrer, C., Bergman, P., 2002. Issues related to seismic activity induced by the injection of CO_2 in deep saline aquifers. J. Energy Environ. Res. 2, 32–46.
Sun, A.Y., Zeidouni, M., Nicot, J.-P., Lu, Z., Zhang, D., 2013. Assessing leakage detectability at geologic CO_2 sequestration sites using the probabilistic collocation method. Adv. Water Res. 56, 49–60.
Tuminaro, R.S., Heroux, M., Hutchinson, S.A., Shadid, J.N., 1999. Official Aztec User's Guide. Massively Parallel Computing Research Laboratory, Sandia National Laboratories.
Walsh, J., 1981. Effect of pore pressure and confining pressure on fracture permeability. Int. J. Rock Mech. Min. Sci. Geomech. Geoeng. Abstr. 18, 429–435.
Wang, S., Xiong, Y., Winterfeld, P., Zhang, K., Wu, Y.-S., 2014. Parallel simulation of thermal-hydrological-mechanical (thm) processes in geothermal reservoirs. In: Stanford Geothermal Workshop, Stanford Geothermal Workshop.
Winterfeld, P.H., Wu, Y.-S., 2012. A novel fully coupled geomechanical model for CO_2 sequestration in fractured and porous brine aquifers. In: XIX International Conference on Water Resources CMWR, pp. 17–22.
Winterfeld, P.H., Wu, Y.-S., 2014. Simulation of CO_2 sequestration in brine aquifers with geomechanical coupling in Computational Models for CO_2 Geosequestration & Compressed Air Energy Storage. CRC Press, pp. 275–303, http://dx.doi.org/10.1201/b16790-12 (Chapter 8).
Wu, Y.-S., Qin, G., 2009. A generalized numerical approach for modeling multiphase flow and transport in fractured porous media. Commun. Comput. Phys. 6 (1), 85–108.
Xu, B., Wong, R.C., 2010. A 3d finite element model for history matching hydraulic fracturing in unconsolidated sands formation. J. Can. Pet. Technol. 49 (4), 58–66.
Zeidouni, M., 2012. Analytical model of leakage through fault to overlying formations. Water Resour. Res. 48 (12).
Zeidouni, M., Pooladi-Darvish, M., Keith, D.W., 2011a. Analytical models for determining pressure change in an overlying aquifer due to leakage. Energy Procedia 4, 3833–3840.
Zeidouni, M., Pooladi-Darvish, M., Keith, D.W., 2011b. Leakage detection and characterization through pressure monitoring. Energy Procedia 4, 3534–3541.
Zhang, J., Standifird, W., Roegiers, J.-C., Zhang, Y., 2007. Stress-dependent fluid flow and permeability in fractured media: from lab experiments to engineering applications. Rock Mech. Rock Eng. 40 (1), 3–21.
Zhang, K., Wu, Y.-S., Pruess, K., 2008. Users guide for tough2-mp-a massively parallel version of the tough2 code. In: Report LBNL-315E. Lawrence Berkeley National Laboratory, Berkeley, CA.
Zhang, R., Yin, X., Wu, Y.-S., Winterfeld, P., et al., 2012. A fully coupled model of non-isothermal multiphase flow solute transport and reactive chemistry in porous media. In: SPE Annual Technical Conference and Exhibition, Society of Petroleum Engineers.
Zhou, Q., Birkholzer, J.T., Tsang, C.-F., Rutqvist, J., 2008. A method for quick assessment of CO_2 storage capacity in closed and semi-closed saline formations. Int. J. Greenhouse Gas Control 2 (4), 626–639.
Zhu, W., Wong, T.f., 1978-2012. The transition from brittle faulting to cataclastic flow: permeability evolution. J. Geophys. Res.: Solid Earth 102 (B2), 3027–3041.
Zoback, M.D., Kohli, A., Das, I., Mcclure, M.W., et al., 2012. The importance of slow slip on faults during hydraulic fracturing stimulation of shale gas reservoirs. In: SPE Americas Unconventional Resources Conference, Society of Petroleum Engineers.